Astron. Astrophys. 247, 434–446 (1991)

ASTRONOMY AND ASTROPHYSICS

Numerical hydrodynamics of counter flowing binary stellar winds

J. Kallrath

Astronomische Institute der Universität Bonn, Auf dem Hügel 71, D(West)-5300 Bonn 1, Federal Republic of Germany

Received September 22, 1990; accepted January 2, 1991

Abstract. The dynamical and geometrical aspects of two quasi radial supersonic counter streaming gas flows are investigated numerically. Analytical approximations of the boundary-layer as an envelope are derived from trajectorial models (two-fixed-centre problem, restricted three-body problem) and pressure equilibrium surfaces derived from an extended Newtonian approximation are used as initial data for the hyperbolic system of equations describing the conservation of mass, momentum and energy. The equations are solved by using a 2-D axial symmetric second order explicit Godunov scheme set up as a finite volume method on a 100×100 grid. By choice of a flux source term we have modeled a free flow pattern, and the flow in the field of the (repulsive) two-fixed centre problem, which is used as a highly simplified model for the radiation field, for a set of parameters of a model (Wolf-Rayet/O) binary. In that test case a subsonic region with an extension of about six solar radii at the head-on collision point is established. The flow pattern visualized as contour plots of density, logarithmic pressure, and Mach number clearly shows the shock fronts and the contact discontinuity. Particularly, the physical parameters within the sub-sonic region are briefly discussed with respect to the possibility of emitting X-ray bremsstrahlung.

Key words: binaries – stellar wind – shock waves – hydrodynamics – Wolf-Rayet

1. Introduction

Under strong radiation pressure the physics of stellar atmosphere and stellar envelopes implies the existence of a radiatively driven wind as observed in O-, B- or WR-stars (Underhill 1986). Typical parameters characterizing such a wind are mass loss rates of $10^{-5} - 10^{-4}\, M_\odot\, \mathrm{yr}^{-1}$ (Doom 1988) and asymptotic wind velocities of about 1000–3500 km s^{-1}. The details of the acceleration mechanism of this wind are not discussed in this paper. If there are two stellar winds in hot (WR + O-star) binary systems as for example V444 Cygni, γ^2 Vel or HD 152 270, one has to model colliding supersonic flows with Mach numbers of about 100 leading to shock- and contact surfaces. Due to the binary stars' orbital motion those surfaces are subject to non-inertial forces. Until now, there has not been any complete hydrodynamical simulation of the boundary-layer concerning its geometrical and physical properties accounting appropriately for shock waves and contact discontinuities.

In some previous works (Kallrath 1989, 1991a), this task, i.e. the *binary stellar wind problem* (BSWP) has been attacked in two first steps in the frame-work of trajectorial models, i.e. the two fixed-centre problem (TFCP) and the restricted three-body problem, and in terms of pressure equilibrium models.

The effect of non-inertial forces in a system like HD 152 270 was found to be responsible for a minor turn of the boundary layer by a small angle of only about 10° against the symmetry line connecting both stars. This result, i.e. the small influence of the non-inertial forces, justifies the use of axisymmetric models for further analysis.

Therefore, in this paper, only the axisymmetric BSWP is attacked by numerical integration of the hyperbolic system of equations describing the conservation of mass, momentum and energy, which govern the stellar wind fluid dynamics. The integration procedure is borrowed from numerical gas dynamics and is capable to model an ideal, compressible gas and to capture shocks and contact discontinuities.

During the last years, the importance of numerical gas dynamics has been increased for the modeling of astrophysical problems (van Albada et al. 1982, VA), e.g. the analysis of mass and angular momentum loss in binary star system (Sawada et al. 1984), the numerical simulation of the interaction between the solar wind and the interstellar medium (Matsuda et al. 1988) or the dynamical modeling of barred spiral galaxies (England 1989). The BSWP has not yet been analyzed with such methods.

The astrophysical problems mentioned above require a numerical algorithm which can treat discontinuities in the fluid distribution. Such "shock-capturing methods" are well known in mechanical engineering problems describing airplane profiles or re-entry problems. In our work we choose the method of Godunov (1959) in its extended second-order (see van Leer 1979 for instance) by giving a piecewise linear distribution of the physical variables within each cell. The procedure is formulated as a finite-volume method. The Godunov method (GM) is a monotone upwind scheme which, in its second-order finite-volume form, is in its efficiency and stability comparable to some more recent algorithms by Osher & Chakravarthy (1983) or the TVD schemes (Yee 1987). It has already been applied in astrophysics for instance to simulate time-dependent cosmic rays (Falle & Giddings 1986) or to investigate shock-cloud interactions in supernova remnants (Falle & Giddings 1987).

Although a steady state solution for the geometry of the interface between both wind flows is expected, the hydrodynamical equations are set up with full time-dependence in Sect. 2.1. They are integrated by a 2$^{\mathrm{nd}}$-order axisymmetric Godunov scheme (Sect. 2.3, 2.4) which advances a given initial solution at $t = t_0$ on a grid through a sequence of time-steps controlled by the *Courant-Friedrichs-Lewy condition* (Courant et al. 1928; Richtmyer & Morton 1967) finally to the steady state character-

ized by constant values of the conserved quantities in each cell. The 1st-order scheme by Godunov (1959) can be derived (Sect. 2.2) in a natural way from the basic conservation laws of mass, momentum and energy written in divergence form enhanced by an equation of state which, in our case, is that of an ideal gas. The discretization leads to a mesh of cells which in cylindrical coordinates (CC) are defined by lines of constant r and constant z parallel and orthogonal to the symmetry axis (SA). The construction of the numerical flux function and its evaluation is based on 1-D sequence of *Riemann problems* each describing the flux across the boundary between adjacent cells. A Riemann problem (Riemann 1892; Chorin 1976; Sod 1978; Menikoff 1989) for a system of conservation laws is an initial value problem with scale-invariant initial data. In one dimension, these initial data consist of distinct constant states on the left and right of a jump discontinuity. The solution is constructed by elementary scale-in-variant waves, i.e. rarefaction waves, shock waves and contact discontinuities.

Eventually, in Sect. 3 we adapt the general formalism of the second-order, axisymmetric explicit Godunov scheme (GS) to the binary system's geometry, and present the initial and boundary data of the partial differential equation system. By choice of a flux source term we model a free flow pattern (S1), and the flow in the field of the TFCP (S2) for a model binary with a set of parameters which might be appropriate to the (WR + O-star) binary HD 152 270. However, this paper is not thought to be an investigation of the individual system HD 152 270. The results are compared with the data derived from the trajectorial analysis and pressure equilibrium surfaces, and the properties of possible X-ray emission in the hard keV band are briefly discussed based on some simple formulae.

2. Numerical gas dynamics based on a second order Godunov scheme

2.1. The basic system of hydrodynamical equations

The fluid motion is governed by the principals of classical mechanics and thermodynamics, and in particular by the conservation laws of mass, momentum and energy. If viscosity effects are neglected, the gas is described by the inviscid Eulerian equations. In an inertial coordinate frame they may be expressed in their integral form:

$$\frac{\mathrm{d}}{\mathrm{d}t}\int_\Omega \boldsymbol{U}\mathrm{d}V+\int_{\partial\Omega}\boldsymbol{n}F\mathrm{d}\Sigma=\int_\Omega S\mathrm{d}V, \tag{2.1}$$

where the column vector $\boldsymbol{U}$ – here written as a transposed row vector –

$$\boldsymbol{U}=[\rho,\ \rho\boldsymbol{v},\ e]^t \tag{2.2}$$

describes the conserved quantities, and

$$\boldsymbol{n}F=\boldsymbol{n}F(U)=[\rho\boldsymbol{n}\boldsymbol{v},\ \rho\boldsymbol{v}(\boldsymbol{v}\boldsymbol{n})+p\boldsymbol{n},\ \boldsymbol{n}\boldsymbol{v}(e+p)]^t \tag{2.3}$$

are the related fluxes. The vector

$$S=[s_\rho,\ s_1,\ s_2,\ s_3,\ s_e]=[s_\rho,\ \boldsymbol{f}_e,\ \boldsymbol{f}_e\boldsymbol{v}]^t \tag{2.4}$$

includes additional source terms for mass, momentum and energy. The terms s_1, s_2 and s_3 may represent momentum source terms of the i^{th} coordinate caused by a transformation of the coordinate frame, e.g. the transformation to cylindrical coordinates. t denotes the time, ρ the density, $\boldsymbol{v}$ the particles' velocity and e is the total energy per unit volume

$$e=\rho\left[\varepsilon+\frac{1}{2}\boldsymbol{v}^2\right], \tag{2.5}$$

where ε is the specific inner energy. Furthermore, p is the thermal pressure, $\boldsymbol{f}_e$ the vector of the external force per unit volume and $\boldsymbol{n}$ is a unit vector normal to the surface $\partial\Omega$. The integral representation of the conservation laws has the advantage, that it does not require the continuity of the dynamical variables, ρ, e and $\boldsymbol{v}$ in space and time. If those fields are differentiable to a required order, then (2.1) may be transformed to an equivalent system of partial differential equations using the divergence theorem

$$\boldsymbol{U}_t+\mathrm{div}\,F=S\Leftrightarrow\partial_t\boldsymbol{U}+\partial_1F_1+\partial_2F_2+\partial_3F_3=S, \tag{2.6}$$

describing the dynamical variables $V:=(\rho,\boldsymbol{v},p)$ in the Eulerian sense as functions of space and time. In Cartesian coordinates x, y and velocity components u, v we find

$$\partial_t\boldsymbol{U}+\partial_xF+\partial_yG=S \tag{2.8}$$

where

$$U=[\rho,\ \rho u,\ \rho v,\ e]^t,\quad F=A(u),\quad G=A(\boldsymbol{v}), \tag{2.9}$$

$$A(X):=[\rho X,\ \rho uX+p\delta_{uX},\ \rho vX+p\delta_{vX},\ (e+p)X]^t. \tag{2.10}$$

For later application we give a specification of the physical source term representing the potential of the restricted three-body problem in the x-y-plane. In the nomenclature of Kallrath (1991b) (Sect. 4, Eqs. 4.14–15),

$$S=\rho[0,\ f_x,\ f_y,\ uf_x+vf_y], \tag{2.11}$$

where f_x and f_y are the force densities in the synodic coordinate frame

$$f_x=2v-x+\mu_1(1-\varepsilon_1)\frac{x-\mu_2}{r_1^3}+\mu_2(1-\varepsilon_1)\frac{x+\mu_1}{r_2^3} \tag{2.12}$$

$$f_y=-2u+y+\mu_1(1-\varepsilon_1)\frac{y}{r_1^3}-\mu_2(1-\varepsilon_2)\frac{y}{r_2^3}, \tag{2.13}$$

ε_1 and ε_2 represent the repulsive part of the $1/r^2$ forces. In addition to this equation one needs an equation of state (EOS) defining the pressure. For ideal gases characterized by the adiabatic index $\gamma=c_p/c_v$ the inner energy

$$\varepsilon=\frac{1}{\gamma-1}\frac{p}{\rho} \tag{2.14}$$

per unit mass leads to the EOS

$$p=(\gamma-1)\left[e-\frac{1}{2}\rho v^2\right]. \tag{2.15}$$

For later application of the axisymmetric BSWP we give the conservation laws in cylindrical coordinates (CC) with coordinates z, r and polar angle φ

$$\partial_tU+\frac{1}{r}\partial_r(rF_r)+\frac{1}{r}\partial_\varphi F_\varphi+\partial_zF_z=S \tag{2.16}$$

where

$$U=[\rho,\ \rho v_r,\ \rho v_\varphi,\ \rho v_z,\ e]^t, \tag{2.17}$$

$$F_r=[\rho v_r,\ \rho v_r^2+p,\ \rho v_rv_\varphi,\ \rho v_rv_z,\ v_r(e+p)]^t, \tag{2.18}$$

$$F_\varphi=[\rho v_\varphi,\ \rho v_r v_\varphi,\ \rho v_\varphi^2+p,\ \rho v_\varphi v_z,\ v_\varphi(e+p)]^t, \tag{2.19}$$

$$F_z=[\rho v_z,\ \rho v_r v_z,\ \rho v_\varphi v_z,\ \rho v_z^2+p,\ v_z(e+p)]^t, \tag{2.20}$$

$$S=[s_\rho,\ g_r+s_r,\ g_\varphi+s_\varphi,\ s_z,\ s_e]^t. \tag{2.21}$$

Note that there occur now some geometrical source terms g_r and g_φ,

$$[g_r,\ g_\varphi]=\frac{1}{r}[p+\rho v_\varphi^2,\ -\rho v_r v_\varphi], \tag{2.22}$$

caused by the transformation to CC. Due to the axial symmetry the system (2.17–22) degenerates and reduces to a 2-D system were all term including derivatives ∂_φ or φ-components drop out leading to formula (3.7–11).

2.2. *The Godunov-scheme (first order)*

The GS is a finite-volume procedure for the numerical modeling of an ideal, compressible gas described by the inviscid Euler equation.

Typical for this and other shock-capturing procedures are its features to start from an initial solution $U(x, t^n)$ at time t^n given on a grid G and advance it to a time $t^{n+1}=t^n+\tau$ using the discretized form of (2.1) or (2.6) on a grid G. Particularly, if there are discontinuities to be expected in the solution, it is advantageous to use the conservation laws (2.1) in their integral representation. Steady state problems are solved by iterating the time-dependent equations towards large time t [Roe & van Leer 1988].

The basic idea of Godunov's method and similar algorithms like those by Osher (1983); Roe (1981) or Roe (1986) is to reduce the interaction at the boundary between adjacent cells to the *Riemann problem* and to describe this problem by discrete wave of finite amplitudes. By doing so one constructs a numerical flux function (Lax 1973).

At each time $t=t^n$ one assumes that there is a constant distribution of the dynamical variables ρ, u, v, e in each cell, i.e. at the boundaries of adjacent cells there are discontinuities

$$U(x, t^n)=\begin{cases} u_{i+1}^n, & i+1>x/\Delta\geq i \\ u_i^n, & i>x/\Delta\geq i-1 \end{cases}, \quad \Delta:=\text{linear size of cell} \tag{2.23}$$

between the i^{th} and $(i+1)^{\text{th}}$ cell. Thus, (2.23) defines a sequence of Riemann Problems (RP). If c denotes the local adiabatic velocity of sound, we note that for sufficiently small τ

$$\tau<\tau_{\max}:=\sigma\frac{h_x}{|u|+c}, \quad \sigma=0.4 \tag{2.24}$$

the solution of the RP associates to a pair of cells cannot yet interact with an adjacent pair of cells. The initial discontinuities decay by shock waves or rarefaction waves, and in the case of non-isothermal gases by contact discontinuities. The RP leads to a system of three transcendental equations. Its solution can be found for instance in Chorin (1976). After its solution is found, the fluxes through the boundaries can easily be calculated according to (2.10–11).

A detailed description of the GS for arbitrary 3-D systems is given by Falle (1991). Basically, the discretization of the system of conservation laws (2.1) leads, after integral averaging in space and time, to an expression, which in cartesian coordinates with a constant ratio $\Delta=V/A$ of volume to surface, for each cell (i, j, k), reduces to

$$U_{ijk}^{n+1}=U_{ijk}^n+\tau S_{ijk}-\tau\frac{1}{\Delta}\sum_i\left[F_i^r-F_i^l\right], \quad \tau:=t^{n+1}-t^n, \tag{2.25}$$

where F_i^l and F_i^r are the area- and time-averaged fluxes crossing the cell-interfaces. The fluxes F_i^l and F_i^r in x-direction, and similar in y- or z-direction, for each cell (i, j, k) are derived from the Riemann problem

$$U=\left.\begin{cases} U_i=U(S_l);\ S_l=(\rho_i, u_i, p_i, e_i), & x\leq x_i \\ U_{i+1}=U(S_r);\ S_r=(\rho_{i+1}, u_{i+1}, p_{i+1} e_{i+1}), & x>x_i \end{cases}\right\}_{jk}. \tag{2.26}$$

If the solution $U^*=U(t=\tau>0, x=0)$ of the RP has been calculated, the fluxes are given by

$$F_x^r=F(U^*) \tag{2.27}$$

and corresponding formulas for F_y^r and F_z^r.

2.3. *The Godunov scheme (second order)*

Originally, the GS was a first-order procedure based on the assumption of constant values in each cell. Procedures of higher order in space need some structure within each cell. Not only the GS, but each upwind procedure of first order can be extended to a second-order procedure in time by applying the first order algorithm to half a time-step, i.e. by calculating $\bar{U}^{n+\frac{1}{2}}$ at time $t^{n+\frac{1}{2}}=\frac{1}{2}(t^n+t^{n+1})$. A more detailed structure within each cell is taken into account by the spatial gradient. In order to avoid numerical problems near shocks, the construction of a second-order procedures requires an averaging function "*ave*", for instance that of VA

$$ave(a, b):=[(b^2+\varepsilon^2)a+(a^2+\varepsilon^2)b]/[a^2+b^2+2\varepsilon^2]. \tag{2.28}$$

Later, a and b will be replaced by components of a gradient vector. ε^2 is a positive number introduced to avoid divisions by zero. The averaging function "*ave*" has the property, that for $a\approx b$ the result is $\frac{1}{2}(a+b)$, while otherwise $\min(a, b)$ is preferred.

Now we can compute the mean gradient of the variables

$$V:=(\rho, \mathbf{v}, p)=(\rho, v_1, v_2, v_3, p) \tag{2.29}$$

in a given cell (i, j, k) at $\hat{x}_i$ for instance in the x-direction by

$$(V_x)_{ijk}:=ave\left[\frac{V_{ijk}^{n+\frac{1}{2}}-V_{i-1jk}^{n+\frac{1}{2}}}{\hat{x}_i-\hat{x}_{i-1}}, \frac{V_{i+1jk}^{n+\frac{1}{2}}-V_{ijk}^{n+\frac{1}{2}}}{\hat{x}_{i+1}-\hat{x}_i}\right]; \tag{2.30}$$

the derivatives in y- and z-direction are calculated similarly. The values $\hat{x}_i$ denote the cell-half points. However, later on in non-cartesian geometries they will be replaced by the mass centres of each cell.

Using the gradients, we can transfer the information from the centre of cell at time $t^{n+\frac{1}{2}}$ to the interface at $x=x_i$ by linear extrapolation. This procedure is performed both, for cell (i, j, k) and cell $(i+1, j, k)$, leading to different states U^l and U^r left and right of the interface

$$U^l=U[V_{ijk}^{n+\frac{1}{2}}+(x_i-\hat{x}_i)(V_x)_{ijk}] \tag{2.31}$$

$$U^r=U[V_{i+1jk}^{n+\frac{1}{2}}+(x_i-\hat{x}_{i+1})(V_x)_{i+1jk}], \tag{2.32}$$

which again, serve as input data for a RP. In x-direction, and analogous in y- and z-direction, the fluxes are again

$$\hat{F}_x^r=F[U^*(U^l, U^r)], \tag{2.33}$$

and the Godunov-step with those values is formally identical to (2.25). Concerning the differences in the construction of the numerical scheme if cylindrical coordinates are used we refer to Falle (1991).

3. Application of the Godunov-scheme to the geometry of binary stars

3.1. The basic equations

In principle, the GA could be applied to the full 3-D set of hydrodynamical equations

$$\partial_t \rho + \mathrm{div}(\rho \boldsymbol{v}) = 0 \tag{3.1}$$

$$\partial_t \boldsymbol{v} + (\boldsymbol{v}\nabla)\boldsymbol{v} = -\frac{1}{\rho}\nabla p + \boldsymbol{f}, \quad \boldsymbol{f} := \boldsymbol{f}_G + \boldsymbol{f}_Z, \tag{3.2}$$

containing the $1/r^2$ force densities

$$\boldsymbol{f}_G := \Gamma_1 r_1^{-3}\boldsymbol{r}_1 + \Gamma_2 r_2^{-3}\boldsymbol{r}_2 \tag{3.3}$$

caused by the gravitation and the repulsive radiation pressure, and the non-inertial force density

$$\boldsymbol{f}_Z := \boldsymbol{\omega} \times (\boldsymbol{r} \times \boldsymbol{\omega}) + 2\boldsymbol{v} \times \boldsymbol{\omega} \quad (\text{'}\times\text{'} \text{ denotes cross product}) \tag{3.4}$$

describing the centrifugal force and the Coriolis force appearing in the synodic coordinate frame. At present, our available computer facilities prevent us from doing so.

Alternatively, according to the argumentation in Kallrath (1991b) we neglect $\boldsymbol{f}_Z$ and make use of the cylindrical symmetry of the problem where z is the coordinate parallel to the line connecting both stars placed at distance d from each other, r denotes the distance of a given point to that line. The polar angle φ does not occur due to the axial symmetry. The WR-star with mass M_1 and the O-component with mass M_2 have positions

$$[z_1, z_2] = \frac{d}{M_1 + M_2}[-M_2, -M_1] \tag{3.5}$$

on the z-axis, i.e. the distances r_1 and r_2 of arbitrary point (z, r) from both stars is

$$r_1 := [(z - z_1)^2 + r^2]^{\frac{1}{2}} =: \frac{z - z_1}{\cos\theta_1},$$

$$r_2 := [(z - z_2)^2 + r^2]^{\frac{1}{2}} =: \frac{z - z_2}{\cos\theta_2}, \tag{3.6}$$

and its line to star i encloses an angle θ_i with the z-axis. In (2.16–22) we remove all quantities related to φ and get the 2-D set of equations

$$\partial_t U + \frac{1}{r}\partial_r(rF_r) + \partial_z F_z = S \tag{3.7}$$

where U, F_r, F_z and S are defined to be

$$U = [\rho, \rho v_r, \rho v_z, e]^t, \tag{3.8}$$

$$F_r = [\rho v_r, \rho v_r^2 + p, \rho v_r v_z, v_r(e+p)]^t, \tag{3.9}$$

$$F_z = [\rho v_z, \rho v_r v_z, \rho v_z^2 + p, v_z(e+p)]^t, \tag{3.10}$$

$$S = [s_\rho, g_r + s_r, s_z, s_e]^t. \tag{3.11}$$

In addition to the geometrical source term

$$g_r = \frac{p}{r} \tag{3.12}$$

caused by the transformation of coordinates, there occurs a physical source term of momentum and energy depending on the force f per unit mass and leading to the total source term:

$$S = [0, g_r + \rho f_r, \rho f_z, \rho(v_z f_z + v_r f_r)]; \tag{3.13}$$

here f_z and f_r denote the projections of the force f per unit mass onto the coordinate axes $\boldsymbol{e}_z$ and $\boldsymbol{e}_r$.

3.2. The choice of the initial data and boundary conditions

In order to apply the GM, a region of the spatial domain of the z-r-plan is decomposed into a $N_z \times N_r$-grid

$$[a^z, b^z] \times [a^r, b^r] = [z_-, z_+] \times [0, R] \to [0, z_+, -z_-] \times [0, R]. \tag{3.14}$$

To avoid complications near the surfaces of both stars, we choose the grid such that

$$z_2 + R_2 < z_- < z_+ < z_1 - R_1, \tag{3.15}$$

holds, where R_1 and R_2 are the radii of the WR-star and the O-component. The number of cells N_z, N_r in both directions is chosen according to the condition

$$\Delta = (z_+ - z_-)/N_z = R/N_r. \tag{3.16}$$

The arithmetic centres and the boundaries of cells are calculated according to

$$\tilde{r}_i = (i - \tfrac{1}{2})\Delta\,\{r_i = i\Delta\}, \quad \tilde{z}_k = (k - \tfrac{1}{2})\Delta\,\{z_k = k\Delta\}. \tag{3.17}$$

The application of the GA requires the specification of some initial distribution $\mathbf{U}_{ik}^1$. If we assume that the procedure will converge towards a unique steady state solution of (3.7), then the initial solution $\mathbf{U}_{ik}^1$ should not be of great importance. However, an initial solution close to the steady state $\mathbf{U}_{ik}^\infty$ we are seeking for, will be very important in order to reduce the amount of computer time needed to integrate (3.7) and advance it in time.

Thus, we choose as initial values $\mathbf{U}_{ik}^1$ those density and velocity fields

$$\boldsymbol{v}_j := \boldsymbol{v}_j(r_j) = v_{j,\infty} f(r_j, R_j)\boldsymbol{e}_{r - r_{xj}}, \quad j = 1, 2, \tag{3.18}$$

$$\rho_j := \rho_j(r_j) = \frac{A_j}{4\pi v_{j\infty}} r_j^{-2} / f(r_j, R_j),$$

$$f(r_j, R_j) := [1 - (R_j/r_j)]^{\frac{1}{2}} \tag{3.19}$$

defined in Kallrath (1991a), where the boundary surface derived in that context distinguishes between points (x, y, z) mainly influenced by star 1 or star 2. In Kallrath (1991a) the quadratically decreasing acceleration field

$$\boldsymbol{a}_j = \boldsymbol{a}_j(r_j) = \frac{1}{2} v_{j,\infty}^2 R_j r_j^{-2}\boldsymbol{e}_{r - r_{xj}}, \quad j = 1, 2, \tag{3.20}$$

enabled us to compare the trajectory and pressure equilibrium models. In order to derive the pressure field, according to Neutsch et al. (1979) we approximate the temperature field by

$$T^4 = [(R_1/r_1)^2 T_1^4 + (R_2/r_2)^2 T_2^4]. \tag{3.21}$$

Now the pressure field

$$p_j(r_j) = p_j^1(\rho/\rho_j^1)^\gamma, \quad p_j^1 = n(\rho_j^1)k T_j^1, \quad j = 1, 2 \tag{3.22}$$

is derived from density and temperature where the reference values are derived from points near to the boundary surface and

used for a global polytropic model. We note, that the procedure is arbitrary to some degree. However, this crude choice of the initial pressure distribution is justified by the fact, that outside the interface the thermal pressure is quite negligible when compared to the kinetic pressure ρv^2; i.e. the energy field (2.5)

$$e_j(r_j)=\frac{1}{\gamma-1}p_j+\frac{1}{2}\rho_j v_j^2, \quad j=1,2 \tag{3.23}$$

is mainly dominated by the kinetic pressure. The complete vector $\mathbf{U}_j$ of conserved quantities now reads

$$\mathbf{U}_j=[\rho_j, \rho v_{rj}, \rho v_{zj}, e_j], \quad j=1,2. \tag{3.24}$$

Let now $r_G(z)$ be the boundary curve numerically derived in Kallrath (1991a) and define an auxiliary function

$$G(z):=\begin{cases}0, & \text{if } z\le z_0=\text{stagnation}\\ r_G(z), & \text{if } z>z_0=\text{stagnation}\end{cases} \tag{3.25}$$

supporting the assignment of the vector $\mathbf{U}_{ik}^1$:

$$\mathbf{U}_{ik}^1=\mathbf{U}_{ik}^*:=\begin{cases}\mathbf{U}_1[r_1\{i,k\}], & \text{if } r(i,k)\le G[z(i,k)]\\ \mathbf{U}_2[r_2\{i,k\}], & \text{if } r(i,k)>G[z(i,k)].\end{cases} \tag{3.26}$$

Those cells (i,k) which intersect with the boundary curve $r_G(z)$ will be treated as dominated by the O-star, i.e. $\mathbf{U}_{2k}^1=\mathbf{U}_1[r_1(i,k)]$.

We now have to supply boundary conditions for the spatial domain $\mathbb{D}$ defined by (3.14). Due to the cylindrical symmetry all fluxes through the z-axis $r=0$ vanish. This is also realized by "reflected symmetry". The external distribution $\hat{\mathbf{U}}_{0k}^n$ is assumed to be a mirror image of $\mathbf{U}_{1k}^n$ in the interior, reflected about the boundary, i.e. for the external cells *('0', k)* adjacent to the boundary holds:

$$\mathbf{U}_{0k}^n=(\rho, \rho v_r, \rho v_z, e)_{0k}^n=(\rho, -\rho v_r, -\rho v_z, e)_{1k}^n=\hat{\mathbf{U}}_{1k}^n,$$
$$0\le k\le N_z+1, \quad n\ge 0. \tag{3.27}$$

Note, that the numeration in k also contains the external "left" and "right" boundary cells. The "left" and "right" boundary of the domain $\mathbb{D}$ should be treated equally. Requiring continuity, we supply "fluid" boundary conditions, i.e. for all times n and $k\in\mathbb{R}_l:=\{-1,0\}$ or $k\in\mathbb{R}_r:=\{N_z+1, N_z+2\}$ we require:

$$\mathbf{U}_{ik}^n=\mathbf{U}_{ik}^*, (1\le i\le N_r+2 \wedge k\in\mathbb{R}_l) \text{ or } (1\le i\le N_{RB} \wedge k\in\mathbb{R}_r). \tag{3.28}$$

It is this requirement which connects the flow field within our numerical domain $\mathbb{D}$ with that close to the stars. Of course, (3.28) makes only sense if the contact discontinuity and the shock curves do not intersect the left or right boundary of $\mathbb{D}$.

At the "top" boundary we assume "free outflow", i.e. we fix boundary conditions with vanishing gradients:

$$\mathbf{U}_{N_r+1k}^n=\mathbf{U}_{N_rk}^n, 0\le k\le N_z+1; \mathbf{U}_{iN_z+1}^n=\mathbf{U}_{iN_z}^n, N_{RB}\le i\le N_R. \tag{3.29}$$

Note, that the system (3.27–29) of boundary conditions describes a grid which in all our applications includes the O-star completely. However, in order to avoid numerical difficulties near the surface of the O-star or physical complications arising by the acceleration mechanism of stellar winds near their origin, i.e. critical points etc., we cut out a region near the O-star leading to the geometry plotted in Fig. 1. This region is defined by three more grid numbers NZ_l+1, NZ_r-1 and NR_u-1 indicating the extreme left, right and top cell of the excluded circle, approximated by rectangle cells. At this circle boundary we supply "fluid boundary" condition, which require for the second order scheme a definition of the gradients, i.e. the next two adjacent cells. The technical details concerning this subject may be found in Kallrath (1989). It might be argued, that it would be more appropriate to choose a grid adapted to the geometrical boundaries. Indeed, there are algorithms which support the transformation of cartesian grids to almost arbitrary geometries (Thompson et al. 1974). However, apart from technical problems, those grids are subject to an unknown influence of the boundary conditions to the whole fluid distribution while in our geometry the boundary influence seems to be more restrained to the boundary region. Furthermore, there are advantages in the treatment of the Riemann problem. Figure 1 shows the grid chosen for our numerical treatment.

In order to check the convergence properties of the numerical integration one needs a well defined criterion. The quantity

$$\delta^n:=\max_{i,k}\{|(\mathbf{U}_{ik}^{n+1}-\mathbf{U}_{ik}^n)/\mathbf{U}_{ik}^n|\}/dt \tag{3.30}$$

seems to be appropriate for this purpose. This operator is applied to each element of the vector $\mathbf{U}_{ik}$. Some care has to be taken when dividing by the elements of $\mathbf{U}_{ik}$ in case there is an element with zero-velocity for instance. In case of convergence the sequence δ^n is monotonically decreasing until it fulfills the condition $\delta^n\approx\delta_\varepsilon$ where the value δ_ε is of the order of 10^{-2}. Besides this numerical test it was more helpful to inspect coloured contour plots giving a global impression of the solution.

3.3. *Numerical simulations and results*

Given typical velocities of the order of 10^8 cm s^{-1}, densities of 10^{-13} g cm^{-3} and pressures of $10^{-1}-10^{+3}$ dyn cm^{-2}, a Courant number of $\sigma=0.4$ and an equidistant grid in r and z of mesh size $\Delta=0.04$ or $\Delta=0.02$ one derives time steps according to (2.24) which are typically of the order of one minute.

According to Neutsch et al. (1979) we choose the set of parameters listed in Table 1 which might be appropriate for the WR/O-star binary HD 152 270. These values are also typical for several others WR/O-binaries. In Doom (1988) we find observed mass loss rates for WR-stars between 10^{-5} and 10^{-4} $M_\odot$ yr^{-1}; Underhill (1986) gives a review of observed temperatures. Similar candidates as HD 152 270 are V444 Cygni and γ^2 Vel (Prilutzki & Usov 1976).

For the parameter set given in Table 1 we computed the solution for a 50 by 50 grid with mesh size $\Delta=0.02$ and another 100 by 100 defined by $\Delta=0.02$. The calculation on both grids were performed both with the physical source term switched OFF (S1) and ON (S2). Already with the first grid we achieved a estimation of the width of the subsonic interface near the z-axis of about $7R_\odot$. But it became also obvious that a finer grid was needed.

Color contour plot of the solutions on the 100 by 100 grids are available from the author and show the density field ρ, the logarithm $\log_{10}p$ of the pressure, $\log_{10}M$ of the Mach number, and the velocity fields v_z, v_r and v. In this paper, in Figs. 2–4, only the contour lines of ρ, $\log_{10}p$ and $\log_{10}M$ can be shown. The shock fronts are clearly seen in those diagrams. They become also obvious in Fig. 5 showing the velocity direction field, representing the solution after 300 121 s. The contact discontinuity is best seen in the density contour plot. With time steps derived

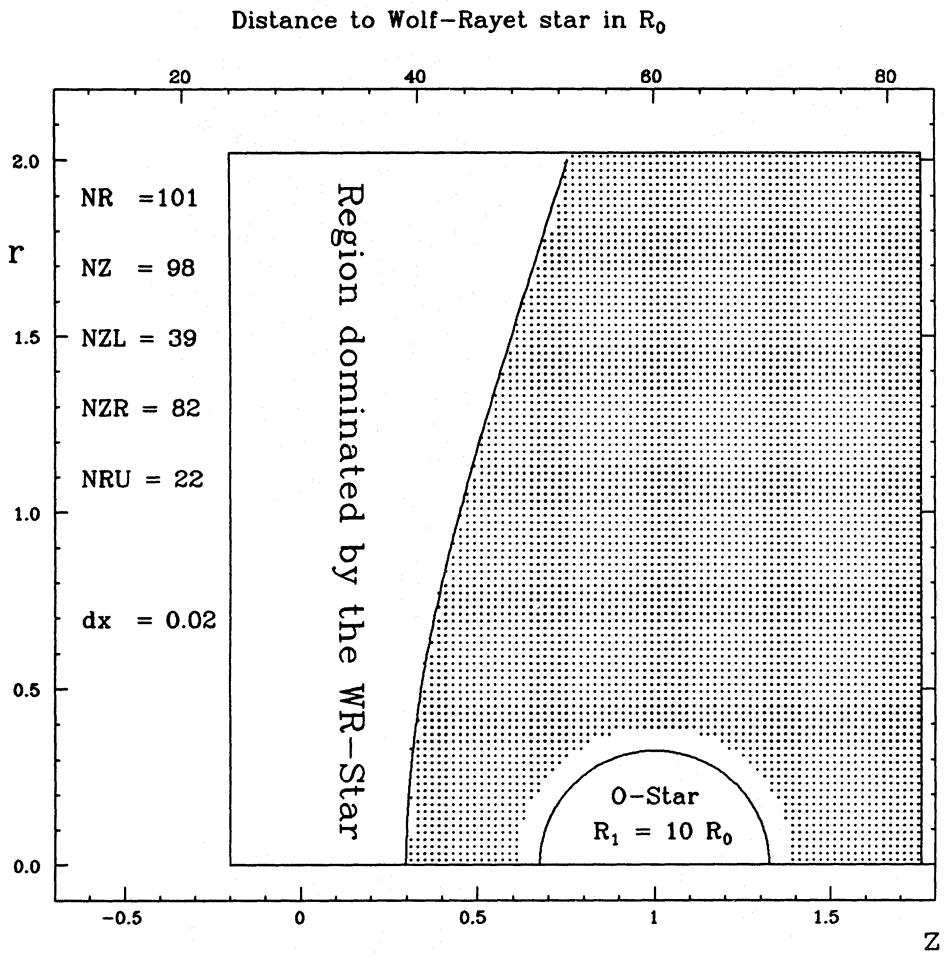

Fig. 1. This figure shows the grid $[-0.2, 1.76] \times [0, 2]$ containing $NR\,NZ$ cells of width dx. The *grey area* around the O-star is, on the left, and limited by the boundary curve derived from a pressure equilibrium model. The initial values within this part of the grid correspond to that distribution of density-, velocity- and pressure-field of an undisturbed O-star stellar wind. The other part, denoted by "Domain of the Wolf-Rayet star" is initially dominated by the Wolf-Rayet star. The numbers *NZL*, *NZR*, and *NRU* characterize a region which is occupied by the O-star and thus is excluded from the grid

Table 1. System parameters for a model (Wolf-Rayet/O-star) binary. The data may be appropriate for HD 152 270 (see Neutsch et al. 1979 and Neutsch 1986)

Binary parameter		
Orbital period	$T = 9^d.107$	
Distance	$d = 60.0\ R_\odot$	
Adiabatic index	$\gamma = \frac{5}{3}$	
	WR-star	O-star
$T/1000$ K	30	40
$R/R_\odot$	12	10
$M/M_\odot$	10	25
ε	8.462	7.249
$A/(10^{-5}\ M_\odot\ \mathrm{yr}^{-1})$	2.221	4.064

from the CFL condition between 1 and 80 (in the average 60, in the final part of the calculations 120 s), we performed about 7000 time steps. Let us now discuss the solution S2 which accounts also for the physical source term caused by the force field (3.3). We will comment on the solution S1 later. Near the z-axis there are nearly normal shocks enclosing a subsonic region of the interface. At greater distances we observe oblique shocks. External to the interface the flow field shows almost radial symmetry. Small deviations are caused by the two-fixed-centre force field.

The width Δ_z of the interface reaches its maximum value at the z-axis and can be "measured" from Figs. 5–7, leading to $6.0\ R_\odot$; the subsonic region extends about $\Delta_r = 25\ R_\odot$ far away from the z-axis. Useful quantities are also the distances $r_{sw} = 30\ R_\odot$ and $r_{so} = 24\ R_\odot$ of both stars to their shocks fronts. The condition $v_z = 0$ in Fig. 6 leads to a distance $r_s = 33\ R_\odot$ of the stagnation point from the WR-star. The strength of the shocks and some further physical data can be extracted from Figs. 6–7 showing the functional relationships $\rho\,(r=0, z)$, $p\,(r=0, z)$, $v_z\,(r=0, z)$, $M\,(r=0, z)$, $T\,(r=0, z)$, and $[\rho v^2 + p]\,(r=0, z=0)$. Actually, these data represent the values of the bottom row of the grid domain $\mathbb{D}$. Attention should also be paid to the temperature distribution. There are temperatures of the order of some 10^7 K. We will comment on that later. Note that the total pressure $\rho v^2 + p$ in Fig. 7 (bottom) is not identical at both shock positions of the interface since the external force also has to be taken into account. In the "free-flow" model discussed below, however, the requirement of equal pressure at both foot points of the interface is fulfilled. This result is the expected one in case of a steady solution since otherwise the interface would move to the left and right. Figures 6–7 also show that the initial distributions in the density and velocity fields outside of the interface are almost conserved identically which proves the quality of the initial flow

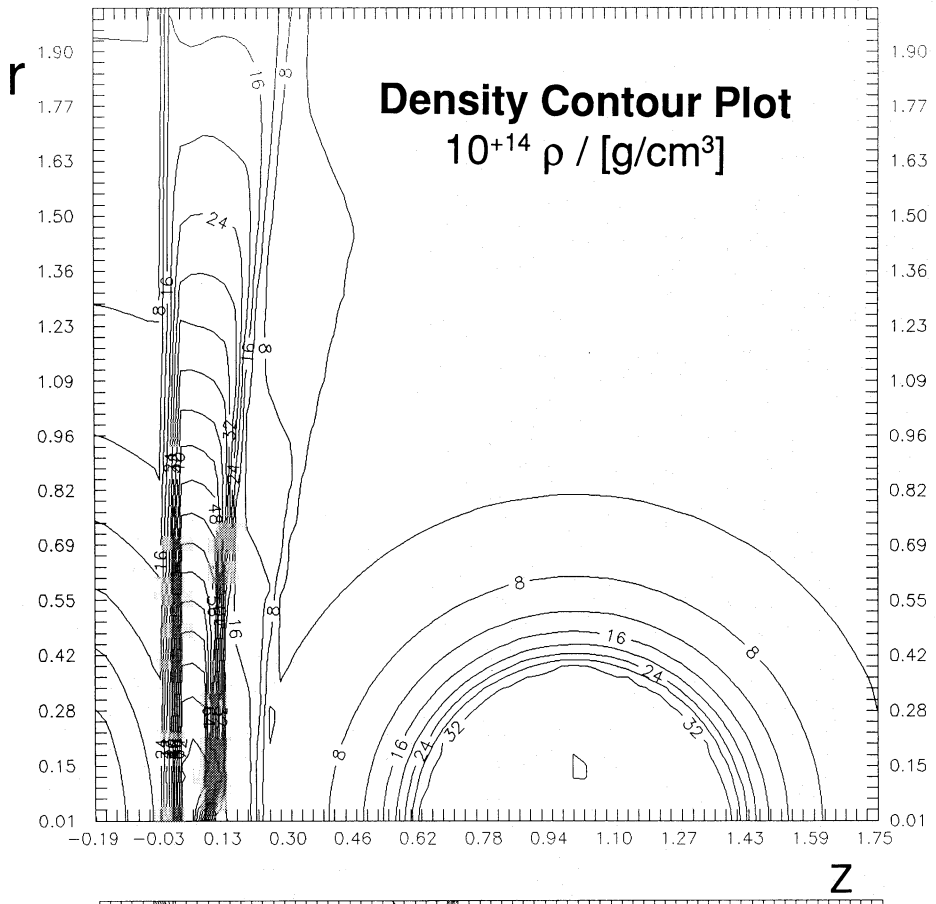

Fig. 2. Contour lines of the density field calculated within the model S2. In the units used in this plots, the interval between adjacent contour lines is 4. The WR-side shock and the contact discontinuity are clearly seen. At $z \approx 0.22$, the O-side shock fronts has its foot point. Note, that in the region dominated by the O-star the radial structure of the density field is almost perfect (some slight deviations are expected from the two-fixed-centre potential

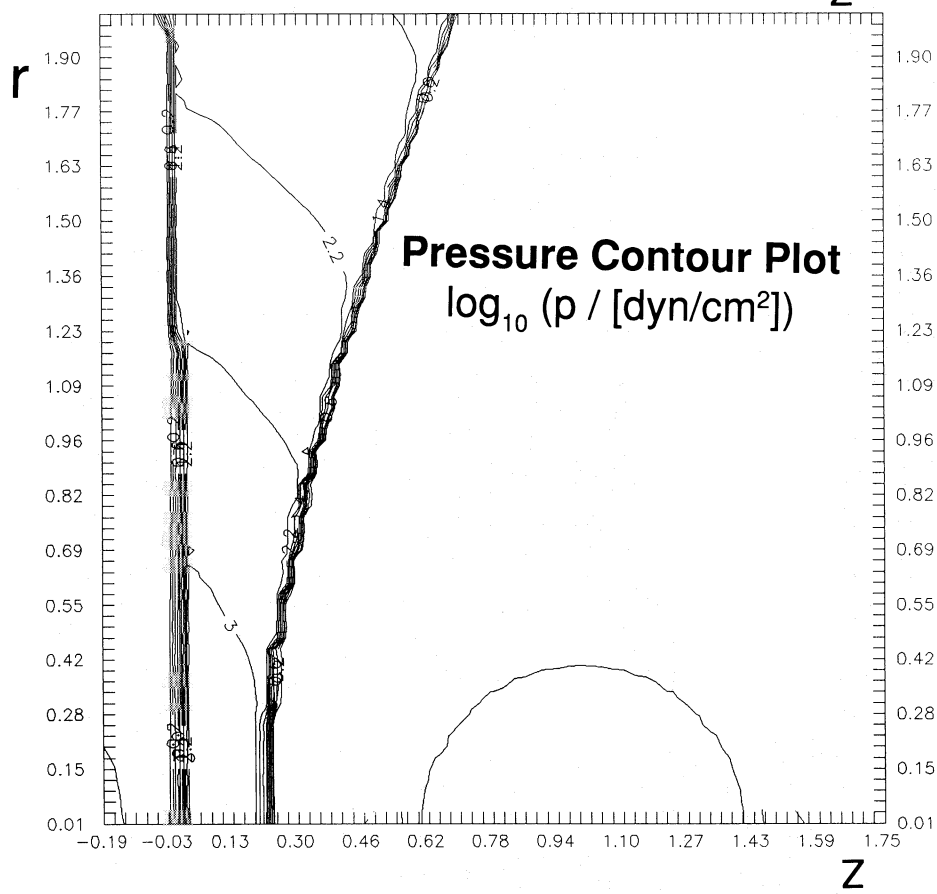

Fig. 3. Contour lines of the pressure field calculated within the model S2. Actually, $\log_{10} p$ is shown. The interval between adjacent contour lines is 0.4. Both shock-fronts are clearly seen. At $z \approx 0.22$, the O-side shock fronts has its foot point

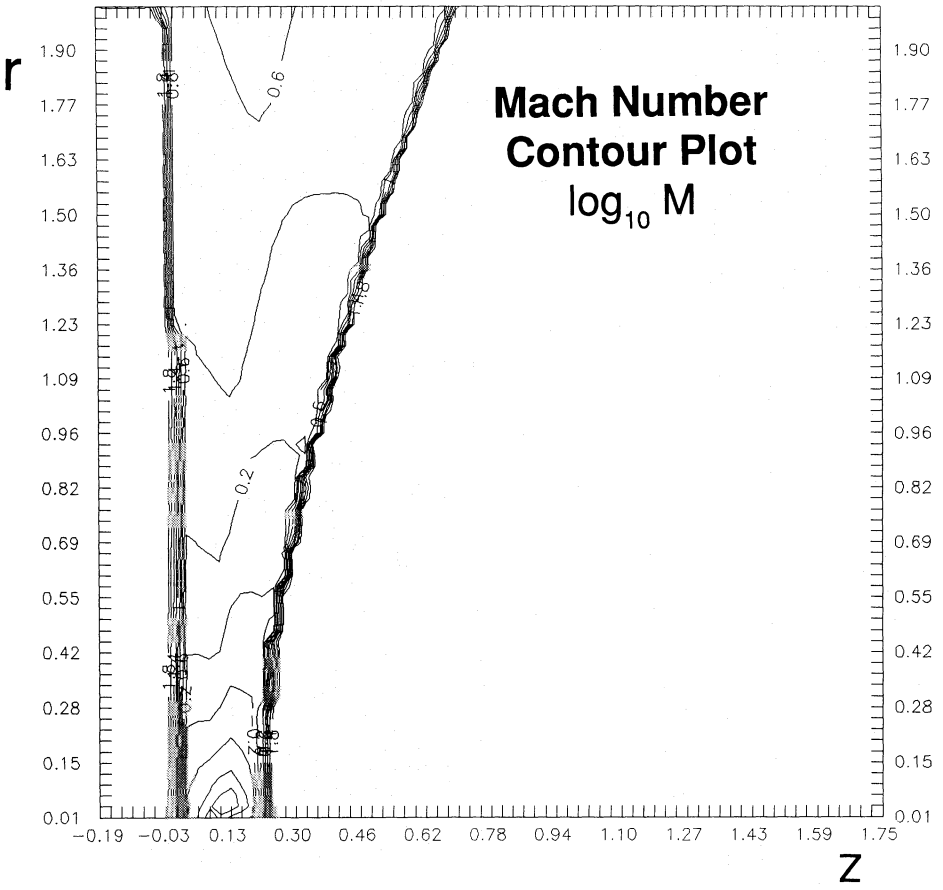

Fig. 4. Contour lines of the Mach number calculated within the model S2. Actually, $\log_{10} M$ is shown. The interval between adjacent contour lines is 0.2. Both shock-fronts are clearly seen. The subsonic region of the boundary interface is limited by the $\log_{10} M = 0$ contour line (not explicitly labeled)

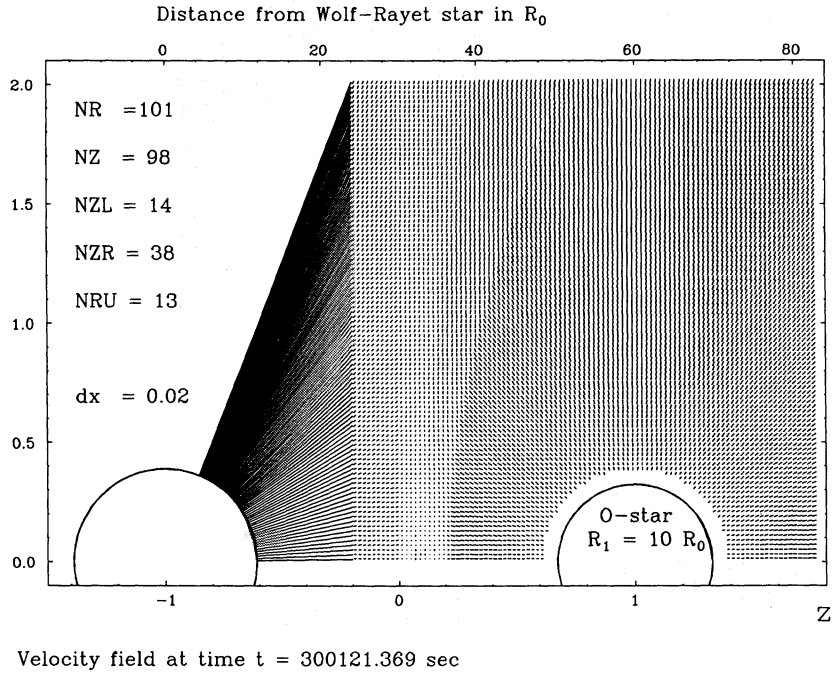

Velocity field at time t = 300121.369 sec

Fig. 5. The flow pattern resulting from S2 is indicated by *small lines* proportional to the absolute value of the velocity. From the shadow effect in this picture the shock surface and the contact surface can be imagined. NR and NZ give the number of cells in the r- and z-direction while dx is the linear size of each cell. The O-side shock front can be easily recognized as a hyperbola. The foot point of the WR-side shock front is approximately at $z = 0.0$ from which the shock front can be traced upwards. The contact discontinuity is also weakly visible in the *upper part* of the figure. The velocities in the upper *right corner* are about 2460 km s^{-1}, those in the *upper left corner* of the grid have values about 1500 km s^{-1}, and the values in the smallest part of the interface are between zero and a few hundreds km s^{-1}

field. Some minor deviations are of course to be expected because of the force field (3.3). The initial distribution of the other profiles are not relevant since the pressure and temperature had been approximated somewhat crudely.

Some caution is required when using the term "steady state". As our frequent inspections of the iterations have shown, the position of the interface and the shock fronts do not change their position and geometry after some time. However, the internal

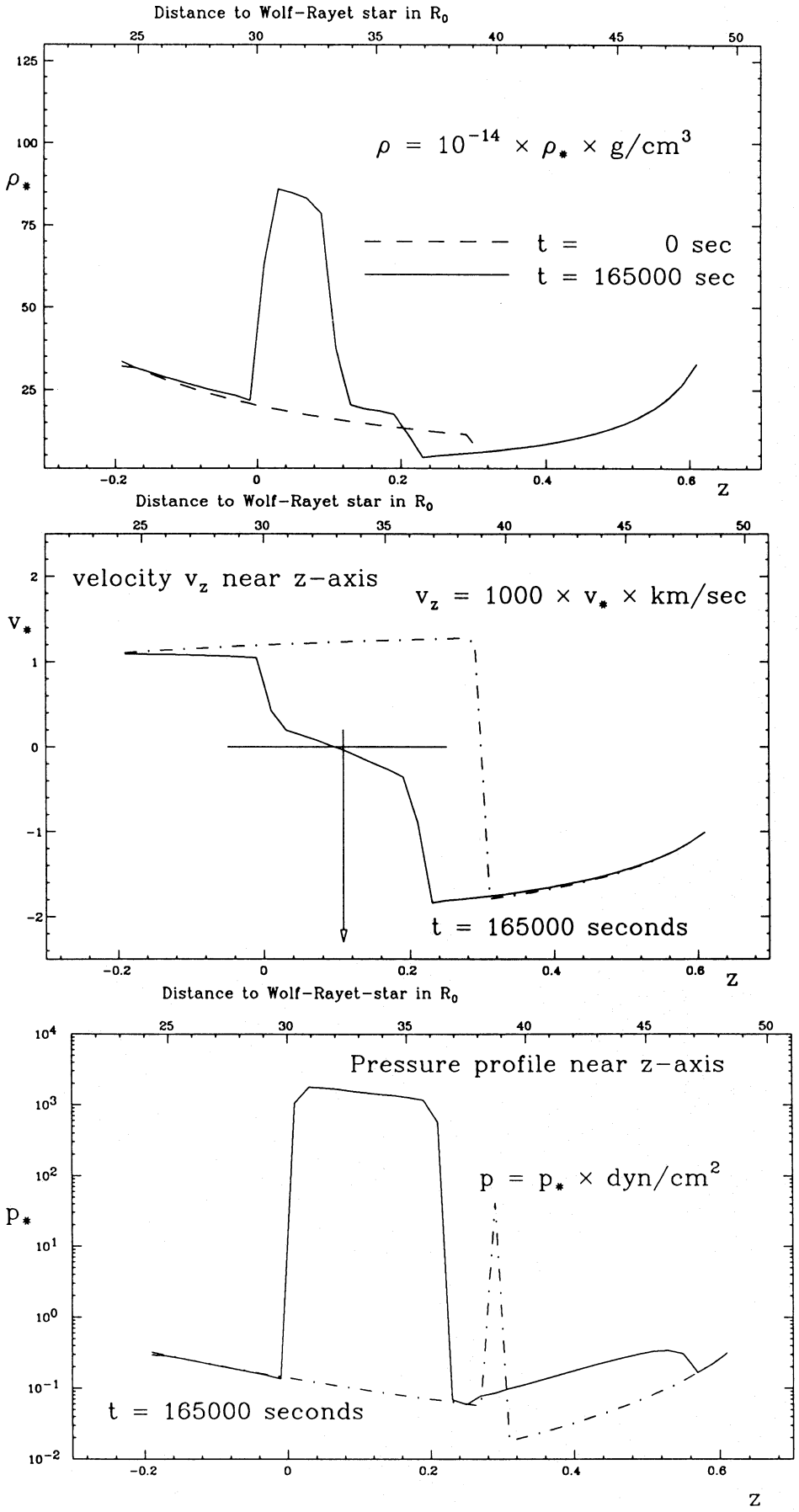

Fig. 6. This picture shows on top the density profile $\rho(r=0, z)$, in the *middle* the velocity profile $v_z(r=0, z)$, and on *bottom* the pressure field $p(r=0, z)$ as derived from S2. From this plots, the strength of the shocks and some relevant physical data can be extracted. Actually, these data represent the values of bottom row of the grid domain $\mathbb{D}$. The *lower axis* shows the dimensionless coordinates while the *upper axis* represents the distance from the WR-star in solar radii. $v_z(r=0, z)$ yields the stagnation point $z_0 = 33\, R_\odot$. There is almost a flat pressure profile within the interface. However, there is some structure of the density profile

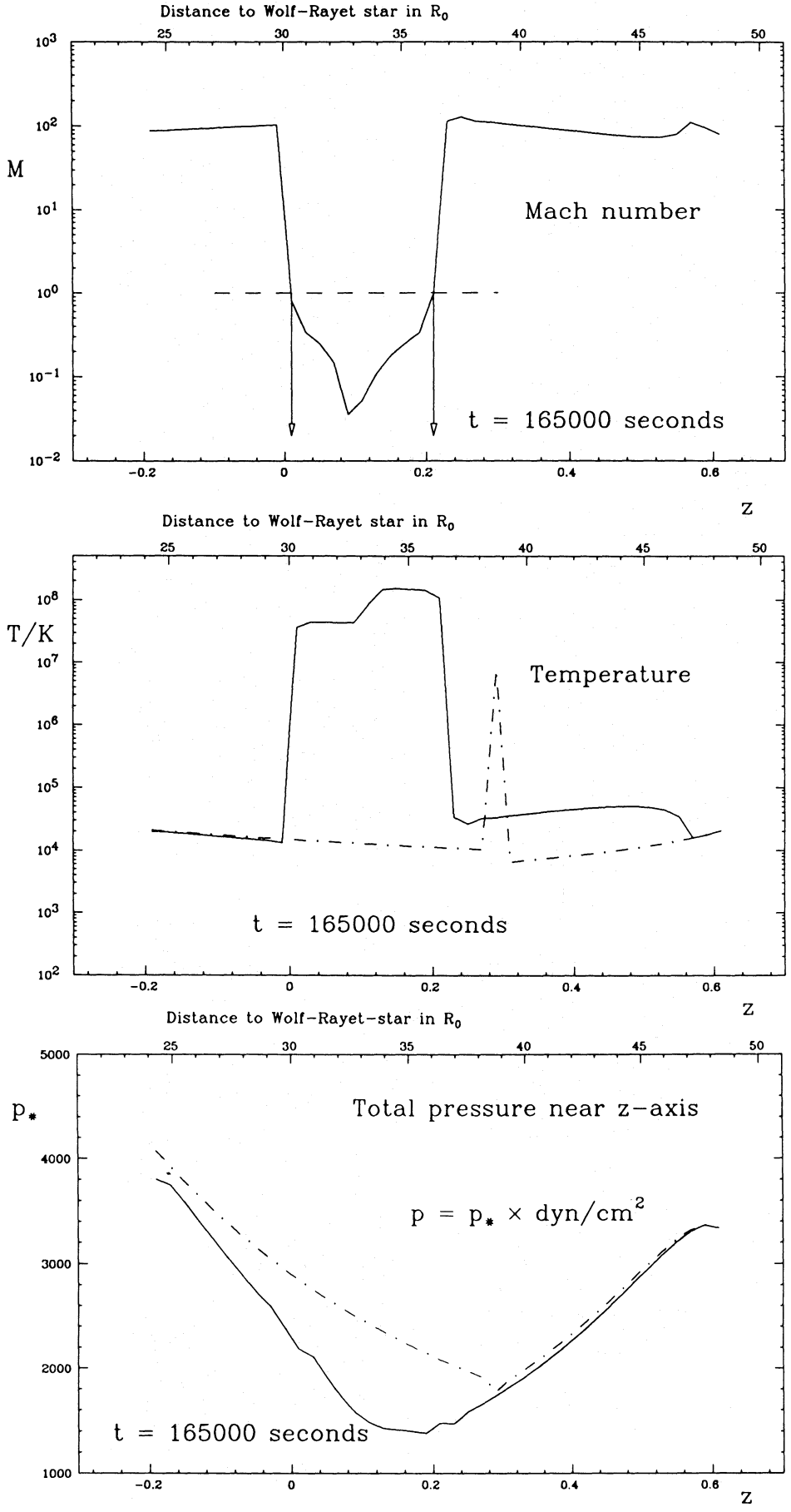

Fig. 7. This picture shows on *top* the Mach number profile $M(r=0, z)$, in the *middle* the temperature profile $T(r=0, z)$, and on *bottom* the total pressure profile $[\rho v^2+p](r=0, z)$ as derived from S2. From the Mach number function, the smallest extension of the interface defined as the subsonic region is derived ($\Delta_z=6.0\,R_\odot$), and the foot points $r_{sw}=30\,R_\odot$ and $r_0=24\,R_\odot$ are also extracted. Between the contact surface and the O-side shock front the temperature profile is almost isothermal. In this picture the total pressure is not equal at both shocks as is expected for a steady state solution. However, the sum of the total pressure and the external forces acting on the interface is equal on both sides of the interface

structure of the interface visualized by the profiles near the z-axis shows some small variations in the density and velocity distribution. In particular, the contact surface varies its position. At this stage of the numeric we refrain from discussion turbulence effects and instabilities within the interface and the question whether a steady contact discontinuity can exist.

Before achieving the solution S2 we also calculated the "free flow" solution S1. If the physical source term is not taken into account, the stellar wind material flows with supersonic velocities at the left boundary of the domain $\mathbb{D}$ and from the approximated O-star's surface into the grid. From then on the fluid moves force-free. We now briefly discuss the differences between the solutions S2 (source flow) and S1 (free flow):

Position of the interface: In S2 the interface is somewhat moved away from the O-star. This is also true for the stagnation point. Both effects are caused by the acceleration field.

Extension of the interface: The intersection points r_{sw} and r_{so} of z-axis move closer to each other, i.e. in S2 the width of the interface is smaller than in S1. This statement holds even more in greater distance from the z-axis, i.e. the external force compresses the interface.

Strcuture of the interface: While in S1 the interface develops almost constant profiles in density, pressure and temperature near the z-axis, i.e. shows isothermal features, in S2 the contact discontinuity becomes very obvious as shown in Figs. 3–4.

Flow profile: In S1 both shock fronts may be approximated by hyperbolas. The shock front next to the WR-star, is in S2 however nearly a straight line normal to the z-axis, and slightly benched to the left in the upper part. External to the interface, in S1, there are constant velocity fields and quadratically decreasing density fields while in S2 those fields are better approximated by (3.18–19) modified somewhat, however, by the two-fixed-centre potential.

Convergence properties: Due to the decreased Courant time caused by the physical source term, the solution S2 required more total time steps to be evaluated. However, it converged already after 70 000 s, while in S1 with averaged time steps of about 60 s the steady state has been achieved after 160 000 s. The steady state refers to the whole interface. It might be the case that a steady contact discontinuity does not exist.

All relevant results of the numerical integration are summarized in Table 2.

3.4. *Discussion of the physical properties of the interface*

The high temperatures of the shocked and heated gas in the interface lead to the question if there is X-ray radiation to be expected from this region. Prilutzki & Usov (1976, PU) and later Bayramov et al. (1988) assume $r_{sw}+r_{so}\approx d$, and give a rough estimation of the total X-ray power L_x, which we review here in somewhat changed appearance:

$$L_x \leq 1.0\,10^{38}\left[\frac{A_{wr}}{10^{-5}M_\odot}\right]^2\left[\frac{r_{so}}{R_\odot}\right]^3\left[\frac{r_{sw}}{R_\odot}\right]^{-4} \times\left[\frac{v_{wr}}{100\ \mathrm{km\,s^{-1}}}\right]^{-1}\ \mathrm{erg\,s^{-1}} \tag{3.31}$$

This formula contains explicitly the mass loss rate A_{wr} of the WR-star and its wind velocity v_{wr} at the WR-side shock front. Since the distances r_{sw} and r_{so} depend on the wind strengths of both stars, all important data of the O-star are implicitly contained in the formula given above. In particular, we learn from Eq. (3.33) that, assuming equal widths of the interface, the X-ray power decreases if the distance of the interface to the O-star decreases. Equation (3.31) holds exactly, if all the energy of the heated gas is converted into X-ray radiation, i.e. if the energy loss caused by matter moving and carrying energy away and other cooling mechanisms may be neglected. In their framework of anaysis, after the shock transition the gas is nearly isotherm and emits free-free X-ray bremsstrahlung of some keV.

Our results concerning HD 152 270 and summarized in Table 2 would lead to $L_x \leq 7.4\,10^{34}\ \mathrm{erg\,s^{-1}}$. Similar computations related to γ^2 Vel and V444 Cygni would result into $L_x \leq 1.2\,10^{32}\ \mathrm{erg\,s^{-1}}$ and $L_x \leq 2.4\,10^{34}\ \mathrm{erg\,s^{-1}}$. All those values should be better interpreted as upper limits since the above formula does not account very appropriately for thermal conduction, i.e. some decrease in $(1<\gamma<\frac{5}{3})$, free-free-radiation in the keV range, expansion or Compton interaction with the radiation field of both stars. More detailed investigations by Cherepashchuk (1976, CH) led to the result, that for binaries with orbital periods between 3 and 100 d and arbitrary mass loss rates there is at most a fraction of $0.3L_x$ emitted in the hard X-ray range, i.e. only a third of the value computed by (3.34).

But we tend to interpret even this value as being to high since the analysis of PU would be more appropriate to the situation of a fluid approaching a solid body. Close to the stagnation point the results derived by PU seem to be best. However, Pollock (1987, PO) points out, that the terrestrial observer has only limited access to this region. Due to photoelectric absorption he usually only receives radiation from regions more distant from

Table 2. The quantities r give the distances of the intersection points of the shock fronts with the z-axis from the Wolf-Rayet star and the O-star, while Δ measures the width or the extension of the interface in z- and r-direction. All these quantities are given in solar radii. The next values refer to the temperatures, densities, pressures and particle densities at the boundaries of the interface and are given ir. units of 10^6 K, $10^{-13}\,\mathrm{g\,cm^{-3}}$, $\mathrm{dyn\,cm^{-2}}$ and $10^{+10}\,\mathrm{cm^{-3}}$. Alternatively, those quantities may also be interpreted as the averaged values of the left and right parts of the interface. Finally, the table also contains the velocity of the WR-wind at the shock front given in $\mathrm{km\,s^{-1}}$ and the X-ray power calculated according to (3.33) in units of $10^{+35}\ \mathrm{erg\,s^{-1}}$

	r_{sw}	r_0	r_{so}	Δ_z	Δ_r	T_{wr}	T_o	ρ_{wr}	ρ_o	p_{wr}	p_o	n_{wr}	n_o	v_{wr}	L_x
S1:	34.5	35.2	16.5	9.0	20	50	50	6.4	6.2	1700	1240	21.4	19.0	1075	14.5
S2:	30.3	33.2	23.7	6.0	25	47	140	8.6	1.9	1770	1170	29.0	5.9	1048	74.3

that part of the interface. Here, photoelectric absorption refers to the effect of carbon or nitrogen atoms in the envelope of the Wolf-Rayet star, the effect of the interstellar medium not taken into account.

Furthermore, a future analysis of this problem should take into account the following physical processes: The conversion of energy into magnetic field energy, emission of synchrotron radiation, and also the energy contained in oscillation of the interface resulting in a continuous compression and expansion of the gas. If magnetic fields are present, then such periodic density- and pressure-oscillations may cause Alfvén-waves leading to a further source of energy loss.

Besides this theoretical considerations we now briefly compare the X-ray powers L_x with those X-ray data observed by the *Einstein-Observatory* and discussed by PO. Those data were derived from observations of 48 WR-stars in the hard X-ray band between 0.8–4 keV and scattered between 10^{32} and 10^{34} erg s^{-1}. One important result was that the X-ray power of (WR + O)-binaries was systematically higher than those values typical for single WR- or O-stars. We believe that the contribution of the interface accounts for this. The measured values for γ^2 Vel and V444 Cygni were $(1.1 \pm 0.1) 10^{32}$ erg s^{-1} and (7.7 ± 1.3) 10^{32} erg s^{-1}. The observed value for HD 152 270 in the 0.2–4 keV band was $(4.4 \pm 4.4) 10^{32}$ erg s^{-1}. This value is certainly lower than the theoretical upper limit discussed above. A similar value was measured for CV Ser. But both measurements have in common that they were achieved at phase $\varphi = 0$, i.e. the WR-star was in front of the O-star. Thus, it is very likely, that the extended envelope of the WR-star hid most of the subsonic part of the interface which leads to an absorption of the X-ray photons by nitrogen or carbon atoms of the envelope. Other observed values of X-ray powers, such as HDE 311 884 or HD 92 470, are related to phase $\varphi = 0.5$, i.e. the O-star was in front. Thus we recommend further observations in the hard X-ray region between 1 and 10 keV and stress, in agreement with CH, the following facts:

(a) If one detects a WR-star with variable radiation in the hard X-ray region of some keV, it is very likely, that this WR-star is a (WR + O)-binary. Apart from Wolf-Rayet-stars, only O- and B-stars are appropriate candidates to fit the required mass loss rates. Theoretical calculations by De Greve et al. (1988) have shown, that (WR + O)-binaries may originate quite easily from mass exchange. The production of (WR + B)-pairs, however, is highly unlikely according to this model.

(b) If a (WR + O)-binary is found, it seems to be worthwhile, to observe such a system in the keV band and cover a complete orbital period.

(c) Simultaneously with the emission of thermal or non-thermal X-rays, according to PO, one should also take into account the emission of non-thermal radio-emission. Similar to the analysis of optical spectra in Neutsch et al. (1979, 1981) or Neutsch (1986), one has to analyze a complex system of dynamical and geometrical effects. In order to analyze the simultaneous variability of photometric, spectroscopic and radio or X-ray data, in an extended model the effects of magnetic fields should be included.

4. Conclusions

Adopting the typical parameters describing the WR- and O-star stellar wind in (WR/O)-binary like HD 152 270 (the stars are 60 $R_\odot$ separated from each other), the numerical integration procedure for the system of equations describing the conservation of mass, momentum and energy uses a zero-order boundary and flow field derived from pressure equilibrium models as initial data and has been applied to constant velocity fields (S1) and fields with quadratically decreasing acceleration (S2) and has yield the following results.

In S2, when compared with S1, the boundary is moved towards the WR-star due to the repulsive force of the O-star. The extension of the subsonic region near the SA is 6 $R_\odot$ in S1, and somewhat smaller, i.e. compressed in S2. The subsonic region extends about 25 $R_\odot$ away from the SA. While in S1 the density, pressure and temperature show almost constant profiles near the SA, in S2 the contact discontinuity is well developed. There are indications that a steady contact discontinuity does not exist; yet at the present state we refrain from discussing that point in more detail. In S1, the shock surfaces are almost hyperboloids with curvature in the same direction, while in S2 the WR-side shock, or its projection on the r-z-plane, is nearly a straight line (see Fig. 1) situated 30 $R_\odot$ away from the WR-star (Kallrath 1989). The physical properties of the interface are characterized by densities of about 10^{-13} g cm^{-3} pressures of 1500 dyn cm^{-2} and temperatures in the region of 10^7–10^8 K. An upper limit for the Bremsstrahlung X-ray power in the hard keV band between 1 and 10 keV is expected to be around 10^{36} erg s^{-1}. This is only in rough agreement with the Einstein observatory data reported by White & Long (1986) of about 10^{32}–10^{34} erg s^{-1} for V444 Cygni, γ^2 Vel and HD 152 270 measured between 0.8 and 4 keV.

The comparison of the geometrical results of our numerical simulation of the boundary-layer does not support the assumption of a zero-thickness interface used in the framework of the NA or similar approaches. Even the smallest width of the interface, realized at the head-on collision point, has a value of about $\Delta_z = 6\ R_\odot$ which is about 10% of the distance of both stars. However, if there are some cooling mechanisms effective in the interface, Δ_z might be reduced simultaneously with an increase of the compression ratio at the contact discontinuity. Finally we note that the foot point of the O-side shock fronts coincidences roughly with the stagnation point derived in the NA.

The Godunov method and the analysis performed in this paper, here applied to an astropause problem of a hot model binary star system, should be applied to some (WR/O) binaries with well known stellar parameters, and may also be used for a study of the heliopause configuration. It looks worthwhile to compare such results with those derived by Baranov et al. (1979) and Matsuda et al. (1989).

Acknowledgements. The author gratefully acknowledges many encouraging discussions with H.-J. Fahr (Institut für Astrophysik, Bonn University) and H. Schmidt (Observatory, Bonn University). Thanks is also directed to S.A.E.G. Falle (School of Mathematics, Leeds University) for his helpful comments on gas dynamics and support concerning the numerical scheme. This work has been generously supported by the Cusanuswerk foundation (Federal Republic of Germany).

References

Bayramov Z.T., Piljugin N.N., Usov V.V., 1988, Astron. Tsirk. 1560, 1

Castor J.I., Abbott D.C., Klein R.I., 1975, ApJ 195, 157

Cherepashchuk A.M., 1976, SvA Lett. 2(4), 138
Chorin A.J., 1976, J. Comput. Phys. 22, 517
Courant R., Friedrichs K.O., Lewy H., 1928, Math. Ann. 100, 32
de Greve J.P., Hellings P., van den Heuvel E.P.J., 1988, A&A 189, 74
Doom C., 1988, A&A 192, 170
England M.N., 1989, ApJ 344, 669
Falle S.A.E.G., Giddings J.R., 1986, MNRAS 225, 399
Falle S.A.E.G., Giddings J.R., 1987, in: Supernova Shells and Their Birth Events, ed. W. Kundt, Lecture Notes in Physics 316, Proceedings, Bad Honnef, Springer, Berlin Heidelberg New York, p. 231
Falle S.A.E.G., 1989 (private communication)
Falle S.A.E.G., 1991, MNRAS 250, 581
Godunov S.K., 1959, Mat. Sbornik 47, 357
Kallrath J., 1989, PhD thesis, Bonn University (FRG)
Kallrath J., 1991a, MNRAS 248, 653
Kallrath J., 1991b, Celest. Mech. (in press)
Lax P.D., 1973, Regional Conference Series in Applied Mathematics 11, Soc. for Industrial and Applied Mathematics, Bristol, p. 1
Matsuda T., Fujimoto Y., Shima E., Sawada K., Inaguchi T., 1989, Progress of Theoretical Physics, 81(4), 810
Menikoff R., 1989, Rev. Mod. Phys. 61, 75
Neutsch W., 1986, Habilitation thesis, Bonn University (unpublished)
Neutsch W., Schmidt H., Seggewiß W., 1979, Veröff. Astron. Inst. Univ. Bonn, p. 98
Neutsch W., Schmidt H., Seggewiß W., 1981, Acta Astron. 31, 197
Osher S., Chakravarthy S., 1983, J. Comput. Phys. 50, 447
Pollock A.M.T., 1987, ApJ 320, 283
Prilutzki O.F., Usov V.V., 1976, SvA 20(1), 2
Richtmyer R.D., Morton K.W., 1967, Finite Difference Methods for Initial Value Problems, Interscience, New York
Riemann B., 1892, 'Über die Fortpflanzung ebener Luftwellen von endlicher Schwingungsbreite' in: Bernhard Riemanns gesammelte MATHEMATISCHE WERKE, p. 256, 2nd edition, Tuebner, Leipzig, p. 156
Roe P.L., 1981, J. Comput. Phys. 43, 357
Roe P.L., 1986, Annu. Rev. Fluid Mech. 18, 337
Roe P.L., van Leer B., 1988, in: Numerical methods for fluid dynamics III, eds. K.W. Morton, M.J. Baines, Clarendon, Oxford, p. 519
Sawada K., Hachisu I., Matsuda T., 1984, MNRAS 206, 673
Sod G.A., 1978, J. Comput. Phys. 27, 1
Thompson J.F., Thames F.C., Mastin C.M., 1974, J. Comput. Phys. 15, 299
Underhill A.B., 1986, PASP 98, 897
van Albada G.D., van Leer B., Roberts W.W., 1982, A&A 108, 76
van Leer B., 1979, J. Comput. Phys. 32, 101
White R.L., Long K.S., 1986, ApJ 310, 832
Yee H.C., 1987, NASA-Technical Memorandum 89464